IOP Publishing Journal of Physics: Condensed Matter
J. Phys.: Condens. Matter **32** (2020) 205503 (8pp) https://doi.org/10.1088/1361-648X/ab6f86

# Titanium nitride halides monolayers: promising 2D anisotropic thermoelectric materials

**Cong Wang**[1] **and Guoying Gao**[1,2]

[1] School of Physics, Huazhong University of Science and Technology, Wuhan 430074, People's Republic of China
[2] Wuhan National High Magnetic Field Center, Huazhong University of Science and Technology, Wuhan 430074, People's Republic of China

E-mail: guoying_gao@mail.hust.edu.cn

Received 18 October 2019, revised 22 December 2019
Accepted for publication 24 January 2020
Published 20 February 2020

**Abstract**

2D graphene-like thermoelectric materials have been extensively explored, however, the studies have mostly focused on the binary compounds and most of them exhibit isotropic electron and phonon transport properties. Here, we investigate the thermoelectric transport properties of ternary TiNX (X = F, Cl, Br) monolayers by using first-principles combined with the Boltzmann transport theory. Both electron and phonon anisotropic transport properties are found. The large *p*-type power factor and the low lattice thermal conductivity along the *y* direction give rise to better thermoelectric performance along the *y* direction than the *x* direction, and the highest *ZT* values at 500 K reach 1.00, 0.89 and 1.17 along the *y* direction in *p*-type doping for TiNF, TiNCl, and TiNBr monolayer, respectively. The anisotropy and the difference of lattice thermal conductivities among TiNX monolayers are discussed in terms of the group velocities, the phonon relaxation time and the three-phonon scattering phase space. These results indicate that TiNX monolayers are promising candidates for 2D anisotropic thermoelectric materials.

Keywords: thermoelectric, phonon transport, 2D materials, titanium nitride halides monolayers, first-principles calculations, Boltzmann transport theory

(Some figures may appear in colour only in the online journal)

## 1. Introduction

Thermoelectric (TE) materials, enabling a direct conversion between heat and electricity, have attracted extensive interests in the context of environmental issue and global warming [1–3]. The performance of TE materials depends on the dimensionless figure of merit $ZT = \sigma S^2 T/\kappa$, where $\sigma$, $S$, $\kappa$ and $T$ are electrical conductivity, Seebeck coefficient, thermal conductivity and temperature, respectively. The thermal conductivity includes electronic ($\kappa_e$) and phonon ($\kappa_l$) parts. Due to the strong coupling among $S$, $\sigma$ and $\kappa_e$, it is difficult to increase the power factor $S^2\sigma$ and decrease the thermal conductivity simultaneously.

During the past few years, some studies have indicated that 2D semiconductors can improve the efficiency of TE materials due to the quantum confinement effect compared to the bulk systems [4–6]. Especially, transition metal chalcogenides (TMDCs) $MX_2$ have been extensively studied both in theory and experiment [1, 7–15]. Searching for new novel 2D TE materials with high power factor and low thermal conductivity by first-principle calculations is a powerful way to significantly enhance the *ZT* value. For example, the metal-shrouded 1T-$Tl_2O$ monolayer predicted by Ma *et al* [16] has been demonstrated to be a potential TE material [17]. Meanwhile, the newly predicted $InP_3$ monolayer not only shows potential applications in photovoltaic solar cells and optoelectronic

 

**Table 1.** The calculated effective mass ($m^*$), elastic modulus $C_{2D}$, deformation potential constant $E_l$, carrier mobility ($\mu$), carrier relaxation time ($\tau$) of electrons and holes along the $x$ and $y$ directions for TiNX monolayers at $T = 300$ K.

| | Carriers | Direction | $C_{2D}$ (eV Å$^{-2}$) | $E_l$ (eV) | $m^*$ ($m_e$) | $\mu$ ($10^3$ cm$^2$ V$^{-1}$ s$^{-1}$) | $\tau$ ($10^{-13}$ s) |
|---|---|---|---|---|---|---|---|
| TiNF | Electron | $x$ | 11.93 | 7.28 | 0.38 | 0.52 | 1.11 |
| | | $y$ | 11.26 | 7.16 | 0.42 | 0.47 | 1.08 |
| | Hole | $x$ | 11.93 | 9.33 | 0.29 | 0.73 | 1.20 |
| | | $y$ | 11.26 | 5.96 | 0.16 | 2.91 | 2.81 |
| TiNCl | Electron | $x$ | 9.08 | 9.79 | 0.15 | 0.87 | 0.74 |
| | | $y$ | 10.14 | 7.11 | 0.41 | 0.67 | 1.56 |
| | Hole | $x$ | 9.08 | 8.40 | 0.14 | 1.55 | 1.32 |
| | | $y$ | 10.14 | 4.46 | 0.26 | 3.68 | 5.22 |
| TiNBr | Electron | $x$ | 8.84 | 9.56 | 0.14 | 1.13 | 0.90 |
| | | $y$ | 10.02 | 7.16 | 0.32 | 0.99 | 1.80 |
| | Hole | $x$ | 8.84 | 9.03 | 0.13 | 1.43 | 1.05 |
| | | $y$ | 10.02 | 3.36 | 0.30 | 4.91 | 8.64 |

devices, but also exhibits promising TE performance with a high $ZT$ of 2.06 [18]. Besides, Peng *et al* took the anisotropic group-V materials (monolayer black phosphorus, $\alpha$-arsenene and aW-antimonenea) as examples to explore how chemical bonds affect the electronic and thermal transport properties [19]. Interestingly, they found that the anisotropic crystal structure, which induces a complex Fermi surface, will attain a low effective mass (high electrical conductivity) and a high density of states (DOS) (large Seebeck coefficient) at the same time. The recently reported anisotropic penta-$PdX_2$ (X = S, Se, Te) monolayers also show high $ZT$ values of 0.85, 1.18 and 2.42 for $PdS_2$, $PdSe_2$ and $PdTe_2$ at 300 K, respectively [20].

The past studies on 2D TE materials most focused on the binary compounds. Recently, ternary layered transition metal nitride halides MNX (M = Zr, Hf, Ti; X = Cl, Br, I) have drawn tremendous attention for optoelectronics, photovoltaics, thermoelectrics and topological properties [21–30]. The structural and electronic properties of bulk TiNX (X = F, Cl, Br, I) have been studied by Altintas *et al* [28]. The TE transport properties of bulk TiNBr was theoretically predicted and the results showed that bulk TiNBr has a large $S$ and a low $\kappa$, e.g. the calculated $\kappa_l$ at 800 K is only 1.34 W m$^{-1}$ K$^{-1}$, and thus a higher $ZT$ of 0.66 was predicted [29]. Meanwhile, further analyses revealed that low phonon group velocity and strong phonon-phonon scattering are responsible for the intrinsic low lattice thermal conductivity. More recently, Liang *et al* predicted that the TiNX (X = F, Cl, Br) monolayers could be obtained from the counterpart layered bulks by mechanical exfoliation or chemical vapor deposition methods, and the optimal bandgap size, superior optical absorption and ultrahigh photoresponsivity make TiNX (X = F, Cl, Br) promising candidates for applications in optoelectronic devices [30]. As far as we know, however, there is rare study on the TE transport properties of these TiNX monolayers. Based on the quantum confinement effect, the anisotropic structural behavior and the exotic optical properties, it is meaningful and urgent to explore how the TE properties of TiNX monolayers and whether they will hold promise as potential TE materials.

In this work, we perform a systematic and comprehensive study on the electron and phonon transport properties of semiconducting TiNX (X = F, Cl, Br) monolayers by using the first-principles calculations and the Boltzmann transport theory. The calculated results show that all the TiNX monolayers are semiconductors with direct band gaps of 1.4–1.57 eV. Both electron and phonon transport properties exhibit remarkable anisotropy, and the transport properties along the $y$ direction are superior to those along the $x$ direction, which can be explained from the calculated electronic band structure and phonon spectrum. Meanwhile, TiNBr has the lowest lattice thermal conductivity among TiNX due to the stronger phonon scattering and the lower group velocity. The optimal $p$-type $ZT$ values along the $y$ direction at 500 K reach 1.00, 0.89 and 1.17 for TiNF, TiNCl and TiNBr monolayers, respectively. The high $ZT$ values and the anisotropy make TiNX monolayers useful in 2D TE applications.

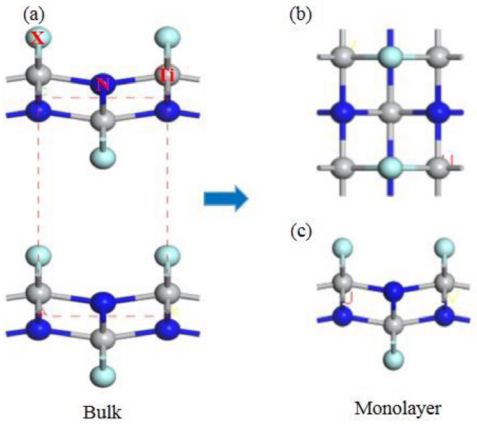


**Figure 1.** The side view of bulk (a), top view of monolayer (b), and side view of monolayer (c) for TiNX (X = F, Cl, Br).

## 2. Computational details

The structural optimization of TiNX (X = F, Cl, Br) monolayers are performed within the framework of density function theory as implemented in the VASP code [31, 32]. The electronic exchange-correlation functional is in the form of Perdew–Burke–Ernzerhof (PBE) with generalized gradient

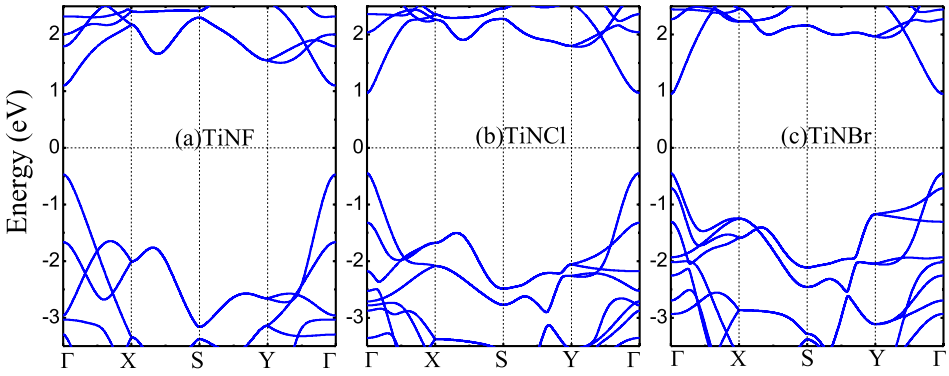


**Figure 2.** The band structures for monolayer TiNX (X = F, Cl, Br).

approximation (GGA) [33]. The cutoff energy for the plane-wave expansion is set to 450 eV, and a Monkhorst–Pack $k$-mesh of $15 \times 15 \times 1$ is used in the Brillouin zone. A 20 Å thickness of vacuum spacing is used along the $z$-axis. As the electronic exchange-correlation potential of GGA usually underestimates the band gaps of semiconductors, we use the screened exchange hybrid Heyd–Scuseria–Ernzerhof (HSE06) [34] functional to calculate the electronic band structure.

After obtaining the electronic band structure, we calculate the electronic transport properties by using the Boltzmann transport theory and the relaxation time approximation (RTA), as implemented in the BoltzTraP code [35], from which we can obtain the $S$ and $\sigma/\tau$. The electrical thermal conductivity is calculated by the Wiedemann–Franz law $\kappa_e = L\sigma T$, where $L$ approaches $1.49 \times 10^{-8}\,\mathrm{W\Omega\,K^{-2}}$ for the nondegenerate semiconductors [36–40]. Unfortunately, although $S$ is independent of the electron relaxation time, $\sigma$ and $\kappa_e$ are calculated with electron relaxation time ($\sigma/\tau$ and $\kappa_e/\tau$) in the BoltzTraP code [35]. The calculation of electron relaxation time $\tau$ is a very trivial task, and $\tau$ is usually treated as a constant extracted from relevant experiments. In this work, we calculate the $\tau$ on the basis of deformation potential theory [41, 42], which has been widely used in some 2D materials [14, 15, 43].

$$\mu = \frac{e\hbar^3 C_{2D}}{k_B T m^* m_d E_l^2}, \tag{1}$$

$$\tau = \frac{\mu m^*}{e}, \tag{2}$$

where $C_{2D}$, $m^*$, $m_d$ and $E_l$ are the effective elastic modulus, the effective mass along the transport direction, the average effective mass calculated by $m_d = \sqrt{m^*_{\Gamma-X} m^*_{\Gamma-Y}}$ and the deformation potential constant, respectively. The calculated $m^*$, $m_d$, $C_{2D}$, $E_l$ and $\tau$ are all listed in table 1.

The phonon thermal conductivity is calculated by solving the phonon Boltzmann transport equation as implemented in the ShengBTE code [44]. The second-order and third-order interatomic force constants (IFCs) for TiNX monolayers are calculated by using a $3 \times 3 \times 1$ supercell with $5 \times 5 \times 1$ $k$-mesh. We impose a cut-off so as to include interactions up to the eighth nearest neighbors for the third order IFCs. For a 2D system, the selection of layer thickness has a great impact on the $\kappa_l$, in our work, we apply the interlayer separation of the bulk TiNX (7.87 Å, 7.80 Å and 8.33 Å for TiNF, TiNCl and TiNBr), and this method has been adopted in the other 2D monolayers [18, 43, 45]. Finally, a $37 \times 37 \times 1$ $q$-mesh is selected to sample the corresponding phonon wave-vector mesh in the ShengBTE calculations [44].

## 3. Results and discussion

### 3.1. Electronic structure and electron transport properties

Bulk TiNX (X = F, Cl, Br) belong to the orthorhombic structure with the space group $P$mmn (figure 1(a)). The crystal structure of TiNX monolayer is shown in figure 1(b). The optimized lattice constants $a/b$ are 3.06/3.99, 3.27/3.98 and 3.38/3.98 Å for monolayer TiNF, TiNCl and TiNBr, respectively, which agree well with the previous theoretical values [30], and are close to the experimental bulk in-plane values [22]. We firstly calculate the electronic band structure based on the optimized lattice. It can be clearly seen from figure 2 that all the TiNX monolayers are semiconductors with direct band gaps of 1.57, 1.42 and 1.40 eV at the Γ point for TiNF, TiNCl and TiNBr monolayers, respectively, which are consistent with the values reported by Liang *et al* [30]. Because accurate band structure and energy gap are crucial to obtain the electronic TE coefficients such as the Seebeck coefficient and the electrical conductivity, the following electronic transport properties for TiNX monolayers are all based on the results of HSE06 [34].

The effective mass $m^*$ on the valence band maximum and conduction band minimum is a meaningful parameter for the thermal transport obtained from the energy band calculation by the equation

$$\frac{1}{m^*_\alpha} = \frac{1}{\hbar}\frac{\partial^2 E(k_\alpha)}{\partial^2 k_\alpha}. \tag{3}$$

Here, $\hbar$ represents the reduced Plank's constant, $E(k_\alpha)$ is the energy determined by the wave vector $k$ and the band index $\alpha$. The calculated effective masses of holes and electrons along the $x$ and $y$ directions are listed in table 1. Clear anisotropy can be found for the effective masses of these monolayers. For example, the calculated effective masses of electrons and holes along the $y$ direction are larger than those along the $x$ direction, which is due to the different dispersion of band

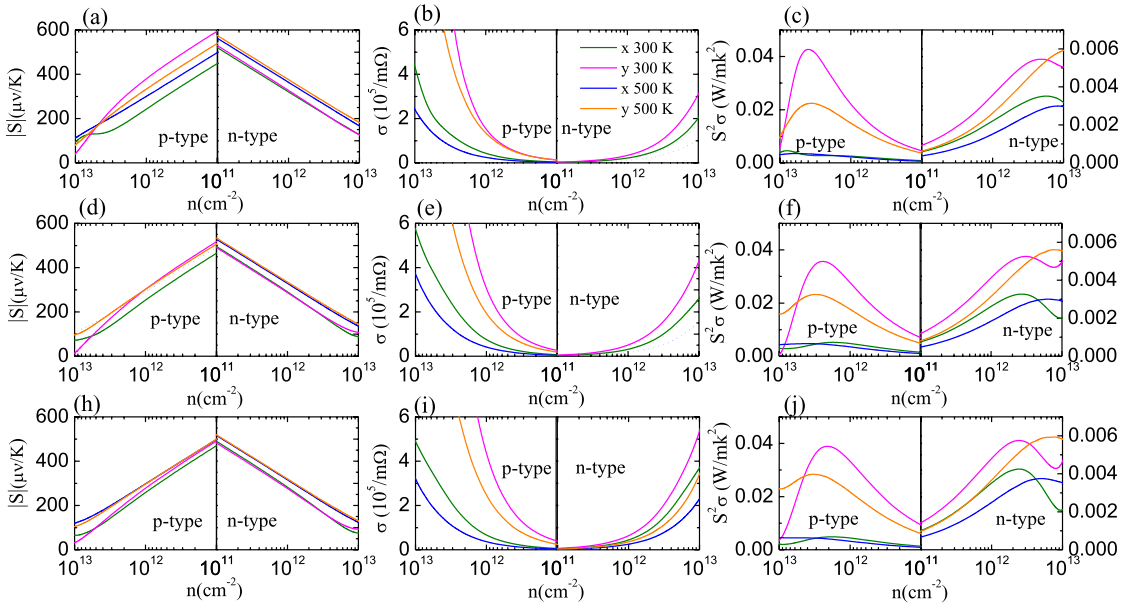


**Figure 3.** The calculated $S$, $\sigma$, $S^2\sigma$ of monolayer TiNF (a)–(c), TiNCl (d)–(f) and TiNBr (h)–(j) along the $x$ and $y$ directions as a function of carrier concentration at 300 K and 500 K.

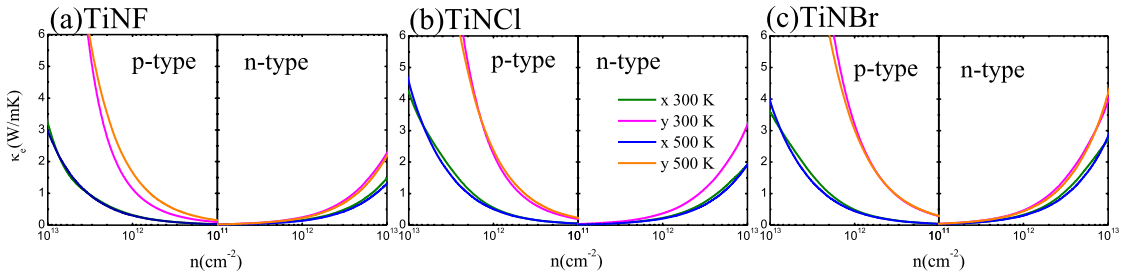


**Figure 4.** The calculated electronic thermal conductivity of monolayer TiNX (X = F, Cl, Br) along the $x$ and $y$ directions for both $p$-type and $n$-type as a function of carrier concentration at 300 K and 500 K.

structures along the different directions. Usually, the distinct dispersive band results in the small effective mass. Besides, the effective masses of electrons are typically higher than those of holes along the same direction. The anisotropic effective masses will lead to the different carrier mobility and electrical conductivity along different directions.

Based on the calculated band structures, we now discuss the calculated electronic transport properties for TiNX monolayers, e.g. the Seebeck coefficient, the electrical conductivity, the power factor and the electrical thermal conductivity. We simulate the doping using the rigid band approximation. The calculated $S$, $\sigma$ and $S^2\sigma$ for TiNX monolayers with the change of carrier concentration $n$ at 300 K and 500 K are shown in figure 3. Both $p$-type doping and $n$-type doping show a large $S$ within a reasonable carrier concentration, which is advantageous to realize considerable $ZT$ values [46, 47]. With the fixed carrier concentration and temperature, the $S$ decreases from TiNF monolayer to TiNBr monolayer, which may be owing to the decrease of the energy gap. In addition, although the calculated effective mass is anisotropic along the $x$ and $y$ directions, the $S$ of $p$-type and $n$-type for these monolayers is nearly isotropic, which is the normal behavior of semiconductors. The calculated $\sigma$ increases with the increase of carrier concentration while decrease with the increase of temperature. And the $\sigma$ in both $p$-type and $n$-type is anisotropic, because the value along the $y$ direction is distinct higher than that along the $x$ direction, due to the different effective masses along the $x$ and $y$ directions. Moreover, the higher hole mobility as a result of the small hole effective mass (table 1) makes the $\sigma$ of $p$-type doping much larger than that of $n$-type doping.

Due to the opposite changes of $S$ and $\sigma$ with the carrier concentration, the power factor $S^2\sigma$ increases first and then decreases with the increase of carrier concentration, and reaches the maximum value with the carrier concentration between $10^{12}$ cm$^{-2}$ and $10^{13}$ cm$^{-2}$. And the $p$-type $S^2\sigma$ is much higher than the $n$-type one, which indicates that better TE performance can be obtained from the $p$-type doping. The maximal $S^2\sigma$ values occur at $T = 300$ K for $p$-type doping along the $y$ direction, which are 0.043, 0.036 and 0.039 W m$^{-1}$ K$^{-2}$ for TiNF, TiNCl and TiNBr monolayers, respectively. What's more, $S^2\sigma$ exhibits remarkable anisotropy. For example, the peak values of $S^2\sigma$ in $p$-type doping along the $x$ and $y$ directions for TiNF monolayer are 0.043 and 0.005 W m$^{-1}$ K$^{-2}$, respectively. The calculated electrical thermal conductivity $\kappa_e$ (figure 4) shows that the $p$-type doping is higher than the $n$-type doping at the same carrier concentration, and the change

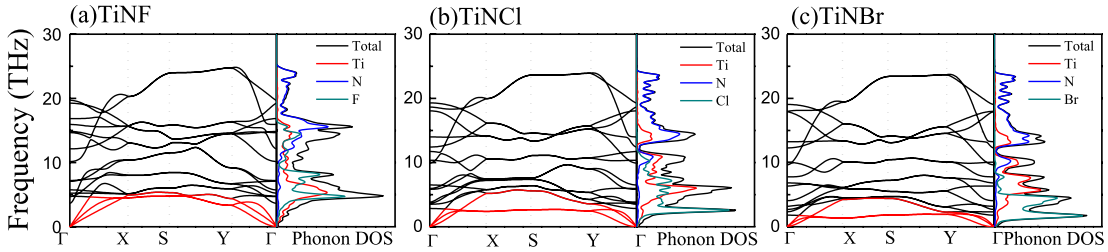


**Figure 5.** The calculated phonon dispersion and phonon DOS for monolayer TiNX (X = F, Cl, Br).

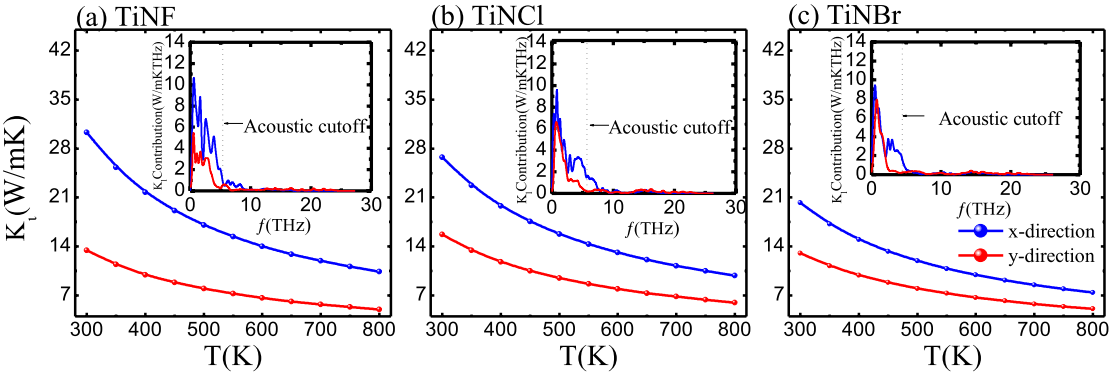


**Figure 6.** The calculated lattice thermal conductivity $\kappa_l$ and $\kappa_l$ contribution with respect to frequency for monolayer TiNX (X = F, Cl, Br).

of $\kappa_e$ with carrier concentration and temperature is similar to that of electrical conductivity.

### 3.2. Phonon transport properties

We now investigate the phonon transport properties of TiNX monolayers. Because each TiNX unit cell contains six atoms, eighteen phonon modes can be found from the calculated phonon spectra (see figure 5). No imaginary phonon frequency emerges, which indicates the stability of TiNX monolayers. The phonon branches move toward lower frequency with increasing mass of the X atom. Meanwhile, the acoustic modes show different dispersion along the Γ–*X* and Γ–*Y* directions, which suggests the anisotropy of phonon thermal conductivity. The calculated total and partial phonon DOS are presented in figure 5. It can be seen that the acoustic modes and low-frequency optical modes originate from the heavy Ti and halogen atoms, while the higher optical vibration modes are afforded by the light N atoms.

The calculated intrinsic $\kappa_l$ of TiNX monolayers as a function of temperature $T$ is plotted in figure 6. For the TiNF monolayer, the calculated $\kappa_\iota$ value at 300 K is 30.30 (13.42) W m$^{-1}$ K$^{-1}$ along the $x$ ($y$) direction, and the corresponding values are 26.74 (15.69) and 20.23 (13.05) W m$^{-1}$ K$^{-1}$ for monolayer TiNCl and TiNBr, respectively. We note that the $\kappa_l$ of monolayer TiNBr is larger than that of the bulk along the $x$ and $y$ directions (about 5 W m$^{-1}$ K$^{-1}$) [29]. The reason may be that, likewise graphite and monolayer graphene [48, 49], for the monolayer form, there is no cross-plane coupling, and the thermal transport mode is of ballistic, which means less collision of phonons. In contrast, there is cross-plane coupling for the layered bulk form, and the in-plane phonons will scatter with those at the neighboring atomic layer, and thus the in-plane thermal conductivity in the bulk will decrease compared to that in the monolayer.

Figure 6 also indicates that lower lattice thermal conductivities can be obtained when the temperature is increased to 800 K. For instance, the $\kappa_l$ value of TiNBr monolayer is only 7.42 (5.06) W m$^{-1}$ K$^{-1}$ along the $x$ ($y$) direction. In addition, the lattice thermal conductivity at 300 K exhibits significant anisotropy with the $k_x/k_y$ ratios of 2.26, 1.70 and 1.55 for TiNF, TiNCl and TiNBr, respectively. It is also easy to find that the difference of $\kappa_l$ between $x$ and $y$ directions for TiNF monolayer is larger than that for TiNBr, which can be explained from the phonon spectra that TiNF monolayer shows more distinct dispersion between Γ–*X* and Γ–*Y* directions. The calculated cumulative $\kappa_l$ (figure 6) with respect to frequency at room temperature indicates that the acoustic modes account for 80% to the total $\kappa_l$ for these systems. Besides, one can see that the lattice thermal conductivity along the $x$ direction makes more contribution to the total $\kappa_l$ compared to that along the $y$ direction.

To understand the phonon thermal transport process, we further calculate the phonon group velocity and the total phonon relaxation time with respect to frequency as shown in figure 7. Compared with monolayer TiNF, monolayer TiNBr possessing of heavier atomic mass has smaller group velocity especially for the acoustic modes. For the ZA, TA and LA modes, the maximum group velocities for monolayer TiNF are about 3.49, 5.37 and 8.90 km s$^{-1}$, respectively, while the corresponding values are about 3.27, 4.21 and 6.30 km s$^{-1}$ for monolayer TiNBr, which means a lower $\kappa_\iota$ in monolayer TiNBr than monolayer TiNF as shown in figure 6.

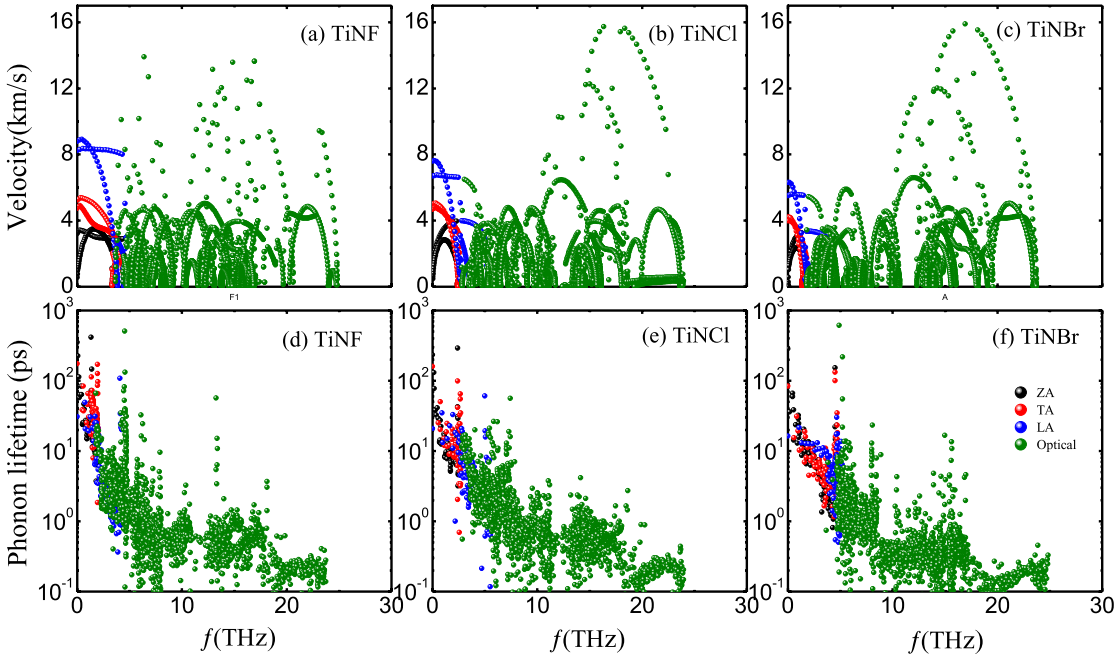


**Figure 7.** The group velocity and phonon relaxation time with respect to frequency for monolayer TiNX (X = F, Cl, Br).

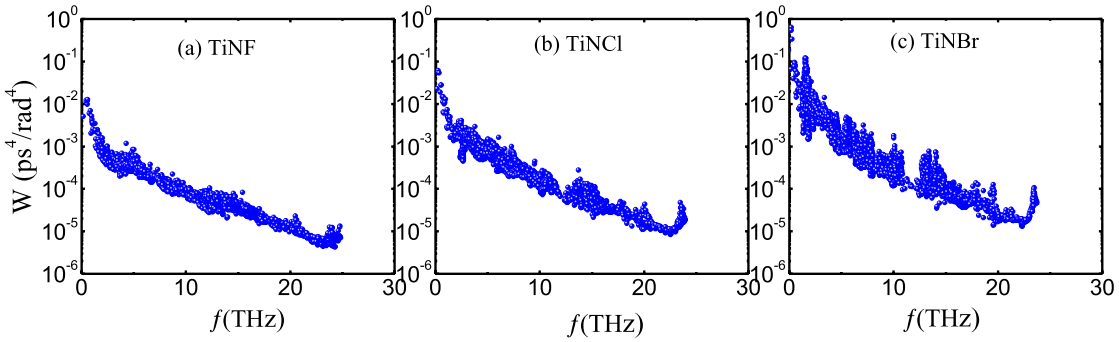


**Figure 8.** The three-phonon scattering phase space $W$ at 300 K for monolayer TiNX (X = F, Cl, Br).

The phonon relaxation time can be obtained from the anharmonic 3rd IFCs, which is inversely proportional to the phonon scattering rate. $2\Gamma_\lambda(\omega_\lambda)$ is the phonon linewidth of the phonon mode $\lambda$, and its reciprocal is the phonon relaxation time $\tau_\lambda$ [50, 51],

$$\tau_\lambda = \frac{1}{2\Gamma_\lambda(\omega_\lambda)}. \tag{4}$$

The form of $\Gamma_\lambda(\omega)$ is analogous to the Fermi golden rule:

$$\Gamma_\lambda(\omega) = \frac{18}{\hbar^2}\sum_{\lambda'\lambda''}\left|\Phi_{-\lambda\lambda'\lambda''}\right|^2\left[\left(f'_\lambda + f''_\lambda + 1\right)\delta\left(\omega - \omega'_\lambda - \omega''_\lambda\right) + \left(f'_\lambda - f''_\lambda\right)\left[\delta\left(\omega + \omega'_\lambda - \omega''_\lambda\right) - \delta\left(\omega - \omega'_\lambda + \omega''_\lambda\right)\right]\right], \tag{5}$$

where $f_\lambda$ is the phonon equilibrium occupancy, and $\Phi_{-\lambda\lambda'\lambda''}$ is the strength of interaction among the three phonons, $\lambda$, $\lambda'$ and $\lambda''$, related to scattering. As can be seen from figure 7, the phonon relaxation times are similar among TiNX monolayers, and the high-frequency optical modes have much shorter relaxation times than the acoustic modes and low-frequency optical modes, which indicates that the acoustic modes account for most of the $\kappa_l$. Besides, the phonon relaxation times for TiNBr monolayer are smaller than those of TiNF monolayer, which means that TiNBr monolayer has stronger phonon scattering than TiNF monolayer. So, the stronger phonon scattering and the lower group velocity give rise to a relatively low lattice thermal conductivity for the TiNBr monolayer than the TiNF monolayer. It should be noted that the higher optical phonon branches exhibit distinct dispersion for these monolayers, which points to higher group velocities of these optical modes. However, they have very low relaxation times, and thus their contributions to lattice thermal conductivity can be ignored.

To further analyze the phonon scattering, we also calculate the three-phonon scattering phase space which represents the number of scattering channels for three-phonon processes, providing insight into the effect of the phonon frequencies on the anharmonic scattering. The three-phonon scattering phase space $W^{\pm}(\omega_\lambda)$ is expressed by [52]

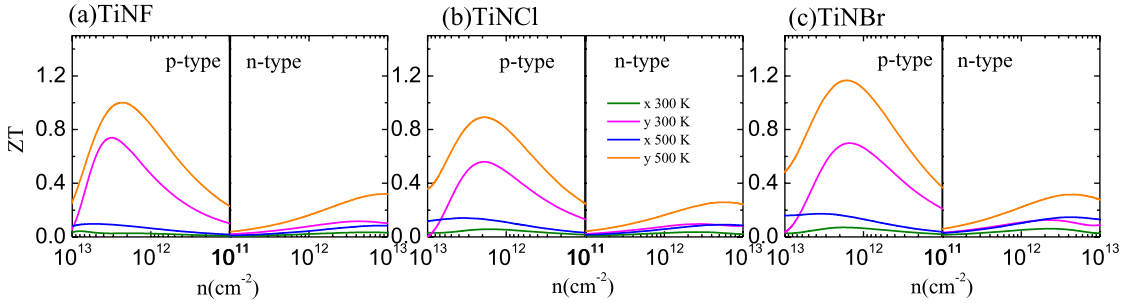


**Figure 9.** The calculated figure of merit (*ZT*) of monolayer TiNX (X = F, Cl, Br) along the *x* and *y* directions in both *p*-type and *n*-type as a function of carrier concentration at 300 K and 500 K.

$$W^{\pm}(\omega_\lambda) = \frac{1}{2N}\sum_{\lambda',\lambda''}\left\{\begin{matrix}2(f_{\lambda'}-f_{\lambda''})\\ f_{\lambda'}+f_{\lambda''}+1\end{matrix}\right\}\frac{\delta(\omega_\lambda \pm \omega_{\lambda'}-\omega_{\lambda''})}{\omega_\lambda\omega_{\lambda'}\omega_{\lambda''}}, \tag{6}$$

where the '+' (' − ') sign represents the absorption (emission) process. It can be seen from figure 8 that the phase space of acoustic modes is on average larger than that of optical modes. Therefore, the acoustic modes have more available channels for phonon scattering processes than the optical modes. In addition, monolayer TiNBr has the largest three-phonon phase space among the three TiNX monolayers, which means the strongest phonon scattering and thus the lowest lattice thermal conductivity for TiNBr among TiNX.

### 3.3. Figures of merit

Finally, based on above results of electron and phonon transport coefficients, we estimate the *ZT* values for TiNX monolayers. Note that a recent work on the *ab initio* MD simulations at 500 K for 1 ps has been performed to confirm the structural stability of TiNX monolayers, which indicates that TiNX monolayers are still thermodynamically stable at 500 K, because there are no structural destruction and broken bonds [30]. So, we mainly estimate the *ZT* values below 500 K. Figure 9 shows the estimated *ZT* values of TiNX monolayers with the change of carrier concentration at 300 K and 500 K. It is easily found that the *ZT* values along all directions in the *p*-type doping are remarkably larger than those in the *n*-type doping due to the better electronic transport performance of holes. Meanwhile, the *ZT* value along the *y* direction is generally superior to that along the *x* direction, exhibiting distinct anisotropy, due to the higher power factor and the lower lattice thermal conductivity along the *y* direction than the *x* direction. The maximum *ZT* values are 1.00, 0.89 and 1.17 along the *y* direction for *p*-type doping at 500 K for TiNF, TiNCl and TiNBr monolayers, respectively, which are comparable to some good 2D TE materials such as monolayer $Bi_2O_2Se$ (1.0 at 500 K) [53] and monolayer $ZrSe_3$ (1.3 at 500 K) [54]. Therefore, TiNX monolayers are promising 2D anisotropic TE materials.

## 4. Conclusion

The recent theoretical studies on monolayer transition metal nitride halides as promising photocatalysts and excitonic solar cells inspire us to investigate the electron and phonon transport properties of TiNX monolayers by using the first-principles calculations plus the Boltzmann transport theory. All three monolayers of TiNF, TiNCl and TiNBr are found to be semiconductors with direct band gaps of 1.57, 1.42 and 1.40 eV, respectively. Interestingly, the *p*-type power factor along the *y* direction is much larger than the *x* direction, and the lattice thermal conductivity along the *y* direction is smaller than the *x* direction, resulting in the remarkable anisotropic transport between *x* and *y* directions. These anisotropic characteristics are explained form the calculated electronic band structure and phonon spectrum. We also discuss the origin of the different lattice thermal conductivities among TiNX monolayers from the calculated group velocity, phonon relaxation time and three-phonon scattering phase space. The estimated *ZT* values at 500 K reach the maximum within the *p*-type doping and along the *y* transport direction, 1.00, 0.89 and 1.17 for TiNF, TiNCl and TiNBr monolayers, respectively, which suggest the potential applications in 2D anisotropic TE materials.

## Acknowledgments

This work was supported by the National Natural Science Foundation of China under Grant No. 11474113.

## ORCID iDs

Cong Wang https://orcid.org/0000-0003-2880-2120
Guoying Gao https://orcid.org/0000-0002-0606-3593

## References

[1] Zhang G and Zhang Y-W 2017 *J. Mater. Chem.* C **5** 7684
[2] Chu S, Cui Y and Liu N 2016 *Nat. Mater.* **16** 16
[3] Aneke M and Wang M 2016 *Appl. Energy* **179** 350
[4] Hsu K F, Loo S, Guo F, Chen W, Dyck J S, Uher C, Hogan T, Polychroniadis E K and Kanatzidis M G 2004 *Science* **303** 818
[5] Biswas K, He J, Blum I D, Wu C I, Hogan T P, Seidman D N, Dravid V P and Kanatzidis M G 2012 *Nature* **489** 414
[6] Guo S-D, Zhang A-X and Li H-C 2017 *Nanotechnology* **28** 445702
[7] Sengupta P, Tan Y, Klimeck G and Shi J 2017 *J. Phys.: Condens. Matter* **29** 405701

[8] Wickramaratne D, Zahid F and Lake R K 2014 *J. Chem. Phys.* **140** 124710
[9] Kumar S and Schwingenschlogl U 2015 *Chem. Mater* **27** 1278
[10] Ding G, Wang C, Gao G, Yao K, Dun C, Feng C, Li D and Zhang G 2018 *Nanoscale* **10** 7077
[11] Bhargavi K S and Kubakaddi S S 2014 *J. Phys.: Condens. Matter* **26** 485013
Peng B, Ning Z, Zhang H, Shao H, Xu Y, Ni G and Zhu H 2016 *J. Phys. Chem.* C **120** 29324
[12] Jena N and De Sarkar A 2017 *J. Phys.: Condens. Matter* **29** 225501
[13] Bhattacharyya S, Pandey T and Singh A K 2014 *Nanotechnology* **25** 465701
[14] Ding G, Gao G Y, Huang Z, Zhang W and Yao K 2016 *Nanotechnology* **27** 375703
[15] Li G, Ding G and Gao G 2016 *J. Phys.: Condens. Matter* **29** 015001
[16] Ma Y, Kuc A and Heine T 2017 *J. Am. Chem. Soc.* **139** 11694
[17] Huang H H, Xing G, Fan X, Singh D J and Zheng W T 2019 *J. Mater. Chem.* C **7** 5094
[18] Ouyang T, Jiang E, Tang C, Li J, He C and Zhong J 2018 *J. Mater. Chem.* A **6** 21532
[19] Peng B, Zhang H, Shao H, Xu K, Ni G, Li J and Soukoulis C M 2018 *J. Mater. Chem.* A **6** 2018
[20] Lan Y S, Chen X R, Hu C E, Cheng Y and Chen Q F 2019 *J. Mater. Chem.* A **7** 11134
[21] Juza R and Heners J 1964 *Z. Anorg. Allg. Chem.* **332** 159
[22] Schurz C M, Shlyk L, Schleid T and Niewa R 2011 *Z. Kristallogr.* **226** 395
[23] Molle A, Goldberger J, Houssa M, Xu Y, Zhang S C and Akinwande D 2017 *Nat. Mater.* **16** 163
[24] Zhang S, Tanaka M, Watanabe E, Zhu H, Inumaru K and Yamanaka S 2013 *Supercond. Sci. Technol.* **26** 122001
[25] Liu J, Li X B, Wang D, Liu H, Peng P and Liu L M 2014 *J. Mater. Chem.* A **2** 6755
[26] Wang A, Wang Z, Du A and Zhao M 2016 *Phys. Chem. Chem. Phys.* **18** 22154
[27] Anand S, Thekkepat K and Waghmare U V 2015 *Nano Lett.* **16** 126
[28] Altintas B 2011 *J. Theor. Comput. Chem.* **10** 65
[29] Zhang S, Xu B, Lin Y, Nan C and Liu W 2019 *RSC Adv.* **9** 12886
[30] Liang Y, Dai Y, Ma Y, Ju L, Wei W and Huang B 2018 *J. Mater. Chem.* A **6** 2073
[31] Blöchl P E 1994 *Phys. Rev.* B **50** 17953
[32] Kresse G and Furthmüller J 1996 *Phys. Rev.* B **54** 1116
[33] Perdew J P, Burke K and Ernzerhof M 1996 *Phys. Rev. Lett.* **77** 3865
[34] Heyd J, Scuseria G E and Ernzerhof M 2006 *J. Chem. Phys.* **124** 219906
[35] Madsen G K and Singh D J 2006 *Comput. Phys. Commun.* **175** 67
[36] Stojanovic N, Maithripala D H S, Berg J M and Holtz M 2010 *Phys. Rev.* B **82** 075418
[37] Toberer E S, Baranowski L L and Dames C 2012 *Annu. Rev. Mater. Res.* **42** 179
[38] Shi X, Yang J, Salvador J R, Chi M, Cho J Y, Wang H and Chen L 2011 *J. Am. Chem. Soc.* **133** 7837
[39] Guo R, Wang X, Kuang Y and Huang B 2015 *Phys. Rev.* B **92** 115202
[40] Wang F Q, Guo Y, Wang Q, Kawazoe Y and Jena P 2017 *Chem. Mater.* **29** 9300
[41] Takagi S I, Toriumi A, Iwase M and Tango H 1994 *IEEE Trans. Electron Devices* **41** 2357
[42] Zhang L C, Qin G, Fang W Z, Cui H J, Zheng Q R, Yan Q B and Su G 2016 *Sci. Rep.* **6** 19830
[43] Zhang J, Liu X, Wen Y, Shi L, Chen R, Liu H and Shan B 2017 *ACS Appl. Mater. Interfaces* **9** 2509
[44] Li W, Carrete J, Katcho N A and Mingo N 2014 *Comput. Phys. Commun.* **185** 1747
[45] Rashid Z, Nissimagoudar A S and Li W 2019 *Phys. Chem. Chem. Phys.* **21** 5679
[46] Yumnam G, Pandey T and Singh A K 2015 *J. Chem. Phys.* **143** 234704
[47] Sun J and Singh D J 2016 *Phys. Rev. Appl.* **5** 024006
[48] Ghosh S, Bao W, Nika D L, Subrina S, Pokatilov E P, Lau C N and Balandin A A 2010 *Nat. Mater.* **9** 555
[49] Zhong W-R, Zhang M-P, Ai B-Q and Zheng D-Q 2011 *Appl. Phys. Lett.* **98** 113107
[50] Togo A, Chaput L and Tanaka I 2015 *Phys. Rev.* B **91** 094306
[51] Ding Y, Xiao B, Tang G and Hong J 2016 *J. Phys. Chem.* C **121** 225
[52] Li W and Mingo N 2014 *Phys. Rev.* B **90** 094302
[53] Yu J and Sun Q 2018 *Appl. Phys. Lett.* **112** 053901
[54] Zhou Z, Liu H, Fan D, Cao G and Sheng C 2018 *ACS Appl. Mater. Interfaces* **10** 37031